scientific reports

Check for updates

OPEN

Microglial TLR4-Lyn kinase is a critical regulator of neuroinflammation, Aβ phagocytosis, neuronal damage, and cell survival in Alzheimer's disease

Rezwanul Islam[1,2], Hadi Hasan Choudhary[1,2], Feng Zhang[1,2], Hritik Mehta[1,2], Jun Yoshida[1], Ajith J. Thomas[1,3] & Khalid Hanafy[1,2,4]✉

Disease-Associated Microglia (DAM) are a focus in Alzheimer's disease (AD) research due to their central involvement in the response to amyloid-beta plaques. Microglial Toll-like receptor 4 (TLR4) is instrumental in the binding of fibrillary amyloid proteins, while Lyn kinase (Lyn) is a member of the Src family of non-receptor tyrosine kinases involved in immune signaling. Lyn is a novel, non-canonical, intracellular adaptor with diverse roles in cell-specific signaling which directly binds to TLR4 to modify its function. Lyn can be activated in response to TLR4 stimulation, leading to phosphorylation of various substrates and modulation of inflammatory and phagocytosis signaling pathways. Here, we investigated the TLR4-Lyn interaction in neuroinflammation using WT, 5XFAD, and 5XFAD x Lyn$^{-/-}$ mouse models by western blotting (WB), co-immunoprecipitation (co-IP), immunohistochemistry (IHC) and flow cytometric (FC) analysis. A spatial transcriptomic analysis of microglia in WT, 5XFAD, and 5XFAD x Lyn$^{-/-}$ mice revealed essential genes involved in neuroinflammation, Aβ phagocytosis, and neuronal damage. Finally, we explored the effects of a synthetic, TLR4-Lyn modulator protein (TLIM) through an in vitro AD model using primary murine microglia. Our WB, co-IP, IHC, and FC data show an increased, novel, direct protein–protein interaction between TLR4 and Lyn kinase in the brains of 5XFAD mice compared to WT. Furthermore, in the absence of Lyn (5XFAD x Lyn$^{-/-}$ mice); increased expression of protective Syk kinase was observed, enhanced microglial Aβ phagocytosis, increased astrocyte activity, decreased neuronal dystrophy, and a further increase in the cell survival signaling and protective DAM population was noted. The DAM population in 5XFAD mice which produce more inflammatory cytokines and phagocytose more Aβ were observed to express greater levels of TLR4 and Lyn. Pathway analysis comparison between WT, 5XFAD, and 5XFAD x Lyn$^{-/-}$ mice supported these findings via our microglial spatial transcriptomic analysis. Finally, we created an in vitro co-culture system with primary murine microglial and primary murine hippocampal cells exposed to Aβ as a model of AD. When these co-cultures were treated with our TLR4-Lyn Interaction Modulators (TLIMs), an increase in Aβ phagocytosis and a decrease in neuronal dystrophy was seen. Lyn kinase has a central role in modulating TLR4-induced inflammation and Syk-induced protection in a 5XFAD mouse model. Our TLIMs ameliorate AD sequalae in an in vitro model of AD and could be a promising therapeutic strategy to treat AD.

Keywords Alzheimer's disease, Disease-Associated Microglia, TLR4, Lyn kinase, TLR4-Lyn modulator protein, 5XFAD

[1]Cooper Medical School of Rowan University, Camden, NJ, USA. [2]Department of Neurology, Cooper University Health Care, Camden, NJ, USA. [3]Department of Neurosurgery, Cooper University Health Care, Camden, NJ, USA. [4]Center for Neuroinflammation at Cooper Medical School of Rowan University, 401 Broadway, Camden, NJ 08103, USA. ✉email: hanafy@rowan.edu; hanafy-khalid@cooperhealth.edu

The role of neuroinflammation in Alzheimer's disease (AD) and its impact on the disease progression has been well-characterized by the activation of glial cells, specifically, astrocytes and microglia[1–3]. These cells, when activated, can release pro-inflammatory cytokines and other inflammatory mediators that may exacerbate neurodegeneration[4]. The accumulation of amyloid-beta (Aβ) plaques is a well-established feature of AD and known to induce the activation of microglia, which then release pro-inflammatory cytokines[5,6]. Aβ accumulation can also influence APP processing. Microglial activation may lead to increased APP production, which in turn can lead to more Aβ production. This inflammatory response can contribute to neuronal damage and promote further plaque formation[7–10]. Neurofibrillary tangles (NFTs), aggregates of hyperphosphorylated tau protein, are closely associated with neuronal loss and cognitive decline due to the resultant deformation of neurons resulting in dystrophic neurites[11,12].

Disease-Associated Microglia (DAM) are involved in the neuroinflammatory response seen in neurodegenerative diseases including Alzheimer's disease (AD)[13–16]. DAMs are characterized by the expression of certain markers such as CD11c and Clec7a[17]. DAM activation involves changes in gene expression and cell behavior, which can influence neuroinflammation and neurodegeneration. DAMs may display altered phagocytic activity, cytokine release, and interactions with neurons, contributing to the progression of disease through mechanisms like enhanced Aβ plaque clearance or exacerbation of neuroinflammation[18–20].

Microglial TLR4 is instrumental in the binding and phagocytosis of fibrillary amyloid in AD[21,22]. The TLR4-mediated NF-κB/MAPK activation promotes the production of pro-inflammatory and neurotoxic cytokines (IL-1β, IL-6, and TNF-α)[23]. Consequently, modulation of TLR4 signaling pathways may exert a significant impact on AD pathology, by regulating the inflammatory state of microglia[24]. Direct inhibition of TLR4, however, would not be a prudent approach for the treatment of AD, due to the subsequent immunosuppression. Further, a clinical trial using a general TLR4 inhibitor in severe septic shock failed for this reason[25]. The role of TLR4 in AD neuroinflammation is well known; however, the relationship between TLR4 and non-receptor tyrosine kinases (NRTKs) remains unclear. NRTKs include Src family kinases (SFKs), such as Fyn or Lyn and Syk family kinases (Syk), such as Syk and Zap70[26,27]. Fyn has been implicated in tau phosphorylation and synaptic function and propagates AD pathogenesis. Subsequently, a phase II-a clinical trial of Fyn inhibitor (saracatinib) in AD patients failed due to a variety of reasons; among them were potential off-target effects, difficulty crossing the blood–brain barrier, lack of long-term evidence, increased cardiac dysfunction, and increased atypical pneumonia[28,29]. Recent preclinical studies on Syk demonstrated that microglial Syk activation increased DAM populations, oligodendrocyte precursor cells, and Aβ clearance following the TREM2/Syk/DAP12/PI3K pathway[30–32]. Another pathway, PI3K/AKT/mTOR, is a key intracellular signaling cascade that regulates cell survival, growth, and metabolism. Based on recent evidence, this pathway is activated when microglia are exposed to Aβ and other pathologic AD inclusions such that the microglia adopt an activated state commonly known as a DAM. The transition from microglia to DAM is regulated by microglial Syk[33].

Macrophage Lyn kinase is involved in both agonistic and antagonistic signal pathways[34]. Deletion of Lyn in the macrophages leads to an increased inflammation in response to MyD88-dependent Toll-like receptors, like TLR4[35]. Supporting Lyn's antagonistic role in TLR signaling of dendritic cells, Lyn was found to inhibit Interferon regulatory factor-5 (IRF5) and subsequent activation of the downstream MyD88 effector[36]. On the other hand, Lyn deletion in mast cells leads to reduced inflammation and histamine release[37,38]. With respect to Syk, Lyn can activate Syk through the phosphorylation of DAP12 or can inhibit Syk by dephosphorylating DAP12 through SHIP1 phosphatase activation[33]. We believe that this same microglial inflammation may be involved in the pathogenesis of AD. Thus, we set out to investigate the role of the microglial TLR4-Lyn pathway and how it affects Syk kinase as well as of neuroinflammation, Aβ phagocytosis, and neuronal dystrophy in a 5XFAD mouse model.

Results

TLR4-Lyn co-expression in macrophages within the Alzheimer's mouse brain

To establish the importance of TLR4-Lyn signaling in AD, we first examined the co-expression of TLR4, and Lyn kinase in 6-month-old WT BL-6 compared to 5xFAD mouse brains. Using immunohistochemistry, we found increased co-localization of TLR4 and Lyn kinase, more so in 5XFAD than in WT, Lyn-TLR4 co-localization shown by surface plots (Fig. 1A, B). In addition to increased expression, we next wanted to establish whether there was a direct interaction between TLR4 and Lyn in AD brains versus WT by co-immunoprecipitation (Fig. 1C). For the co-IP, TLR4 was immunoprecipitated and Lyn kinase was pulled down out of mouse brain lysate from WT and AD brains; the results show increased TLR4-Lyn interaction in AD brains versus control. Furthermore, we determined whether the increased expression of TLR4 and Lyn was occurring in the same cell, specifically macrophages. Our flow cytometry data also showed an increased DAMs ($CD11c^{+}Clec7a^{+}$) percentage and $TLR4^{+}Lyn^{+}$ DAM population in 5XFAD mice (Fig. 1D, E). These results indicate that there is a positive correlation between AD pathogenesis, TLR4 expression, and Lyn kinase activity in the brain. Furthermore, AD pathogenesis leads to increased interaction between TLR4 and Lyn.

Lyn controls cell survival signaling by Syk regulation

To confirm the increased activity of the PI3K, AKT, and GSK3β cell survival pathway with the deletion of Lyn kinase, we performed western blots of 6-month-old mouse brain lysates from 5XFAD X Lyn-/-, 5XFAD, and WT mice. Interestingly, we found increased expression of phospho-Syk (activated Syk), PI3K, activated AKT, and phosphorylated GSK3β in 5XFAD X $Lyn^{-/-}$ compared to 5XFAD mice (Fig. 2A, B). Our WB, IHC, flow cytometry data confirmed the Lyn deletion in the 5XFAD X $Lyn^{-/-}$ mice (Fig. 2A-D). Flow data also showed the increased expressions of TLR4 and Syk kinase in the 5XFAD X $Lyn^{-/-}$ mice (Fig. 2D, E). Thus, an inverse relationship exists between Lyn activity and the protective functions of Syk kinase.

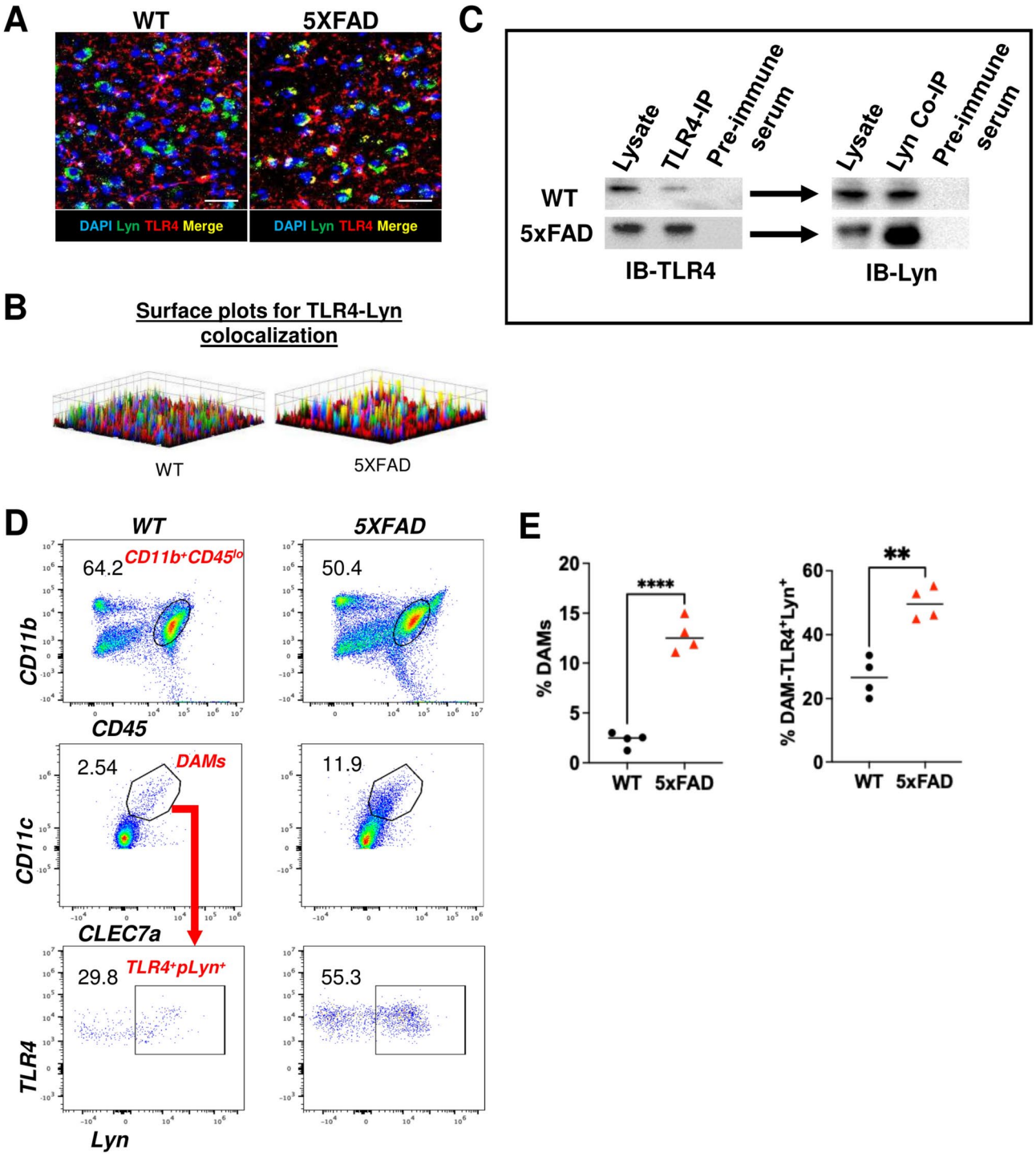

Fig. 1. Macrophage TLR4-Lyn co-expressions in Alzheimer's mouse brain. **a**) IHC imaging of WT and 5xFAD mouse brains for Lyn (1:350; green) and TLR4 (1:500; red). All scale bars = 50 µm. **b**) Surface plots of Lyn-TLR4 colocalization for each group was quantified using ImageJ software, yellow color represents highest possible colocalization. **c**) Co-immunoprecipitation of Lyn kinase and TLR4 to establish direct interaction between the two proteins in AD vs WT mice brains. **d**) DAMs are characterized by $CD11c^{+}Clec7a^{+}$ population plotted on microglia ($CD11b^{+}CD45^{med}$) in mouse brains. Bottom plots show Lyn and TLR4 double positive DAMs. **e**) Quantification of DAMs and the DAM subset that is pLyn and TLR4 double positive. (n = 4; students t-test *P < 0.05, **P < 0.001, ***P < 0.0001 between groups).

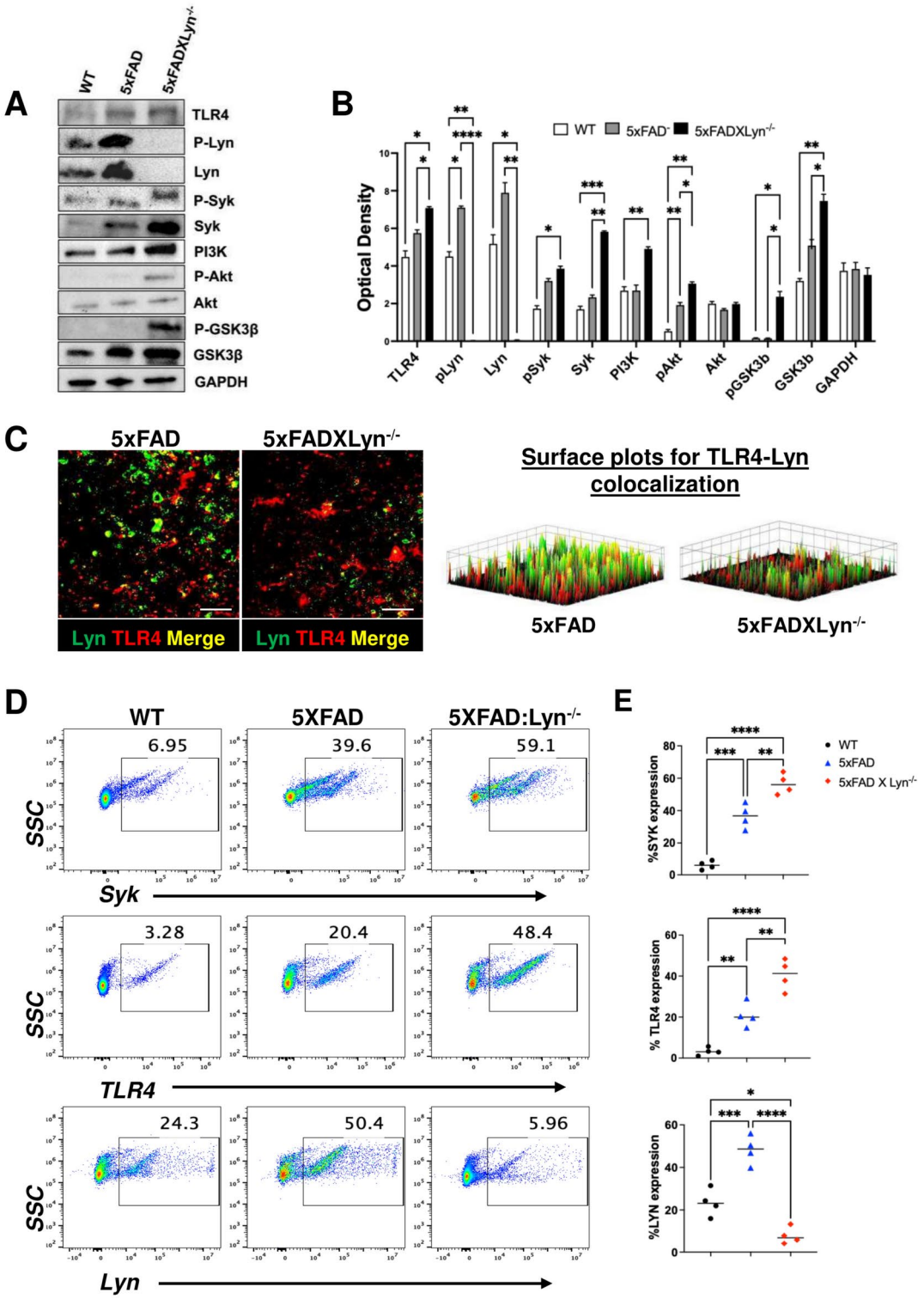

Fig. 2. Cell signaling pathway analysis. **a**) WB of TLR4, pLyn, Lyn, pSyk, Syk, PI3K, pAkt, Akt, pGSK3β, and GSK3β in WT, 5xFAD and 5xFAD X Lyn$^{-/-}$mice, GAPDH was used as loading control. **b**) Quantification of band area of the proteins analyzed by western blot, n = 3; F = 70.34, 99.16, 74.45, 93.51, 76.57, 90.32, 71.08, 52.35, 51.50, 57.97 for all proteins, respectively. F for GAPDH was 1.03 and not significant. One-Way ANOVA, *P < 0.05, **P < 0.001, ***P < 0.0001 between groups. **c**) Immunohistochemical imaging of 5xFAD and 5xFAD X Lyn$^{-/-}$mice for Lyn (1:350; green) and TLR4 (1:500; red). All scale bars = 50 µm. Surface plots of Lyn-TLR4 colocalization for each group was quantified using ImageJ software, yellow color represents highest possible colocalization. **d**) Flow cytometric analysis of Syk, TLR4, Lyn expression on the total brain cells of WT, 5XFAD and 5XFAD X Lyn$^{-/-}$ mice. **e**) Quantification of Syk (F = 75.29), TLR4 (F = 43.56), Lyn (F = 48.15) expression by the brain cells (n = 4; One-way ANOVA *P < 0.05, **P < 0.001, ***P < 0.0001 between groups).

Lyn kinase modulates the glial activation and inflammatory cytokines production by the microglia

Based on the Microglial Morphology Analysis Index (MMAI) that we have previously published, microglia that were more activated had large cell bodies and small, stubby pseudopodia, whereas quiescent microglia had small cell bodies and long, thin pseudopodia[39]. Our MMAI results from the recent study shows that microglia from 5XFAD X Lyn$^{-/-}$ mouse brain are more activated than the WT and 5XFAD (Fig. 3A). To detect the reactive astrocytes, brain slices were stained with GFAP. We found that absence of Lyn kinase made the astrocytes more reactive than the control AD mice (Fig. 3B, C). We next sought to determine the production of TNF-α and IFN-γ by the brain macrophages in WT, 5xFAD and 5XFAD X Lyn$^{-/-}$ mice using flow cytometry. Microglia were gated on CD11b^{+}CD45^{med} population and determined the cytokine production on that population. The highest level of cytokine (TNFα and IFNγ) production was seen in the 5XFAD X Lyn$^{-/-}$ microglia than the other groups (Fig. 3D, E).

Pathway heatmaps analyzed from spatial transcriptomic data

To support the concept that TLR4-Lyn signaling contributes to a more inflammatory profile, we performed unbiased spatial transcriptomic analysis on six 650 µm x 650 µm square regions of interest (ROIs) in coronal slices (supplementary Fig. S1). Analysis of transcriptomic data was done in conjunction with Coriell bioinformatics, and 5xFAD transcriptomes were divided by their sex-matched WT controls to create comparisons between 5xFAD and WT. This normalization allowed us to create pathway-dependent-heat maps (Fig. 4A-C), pathway-dependent primary component analysis (PCA) (Fig. 4D), and volcano plots (Fig. 4E). Interestingly, this includes pathways that focus on cell survival signal pathway (Fig. 4C). As in Fig. 4A, all the genes known to be involved in type II IFN signaling are grouped together and then the relative expressions of those genes based on the cDNAs from the mRNAs in MGs on the brain slide are quantified by color. Pathway-dependent PCA maps are created in a manner that combines neighbor analysis, like that seen in tSNE plots, and the KEGG analysis of heat maps. In the phagocytosis PCA map, important genes known to be involved in this pathway are grouped by similarity, and their importance in the pathway is quantified by the amplitude of the vector. Genes expressed to a greater degree in the 5XFAD X Lyn$^{-/-}$ MG-transcriptome point to the circle on the right. Overall, one can see that both the majority and the critical genes involved in phagocytosis are expressed to a greater extent in the 5XFAD X Lyn$^{-/-}$ MG -transcriptome compared to the 5XFAD-MG-transcriptome. Finally, the volcano plot is not pathway dependent (Fig. 4). These spatial transcriptomics data are helpful in providing a correlative understanding of TLR4-Lyn pathways in inflammation, phagocytosis, and cell survival signaling pathways in 5XFAD X Lyn$^{-/-}$ compared to 5xFAD.

Lyn limits in-vivo phagocytosis in AD

We next sought to investigate the role of Lyn kinase in DAMs and macrophages with respect to AD-induced inflammation, phagocytosis of Aβ, and AD-induced neuronal injury. To accomplish this, we performed flow cytometry of the brain cells from 6-month-old 5xFAD mice intraperitoneally treated with Methoxy-X04, a blood–brain barrier permeable fluorescent probe for detecting amyloid beta plaques[40]. IHC staining with Iba-1 of the brain slices showed the engulfment of Me-X04 tagged Aβ, which is higher in 5XFAD X Lyn$^{-/-}$ compared to control 5XFAD (Fig. 5A, B). Flow-cytometry data shows that Lyn deficiency increased DAM population by 1.5 times compared to the control 5XFAD group. A significant increase in the microglial phagocytosis also observed in the Lyn deficient 5XFAD mice compared to the control 5XFAD (Fig. 5C, D). Results suggest that loss of Lyn increased significant number of DAMs and also increased microglial phagocytosis in Alzheimer's disease.

Lyn deficiency improves neuronal damage and cognitive dysfunction

To ascertain Lyn's role in neuronal damage and cognitive function, WT, 5XFAD, and 5XFADXLyn$^{-/-}$ mouse brains were stained with amyloid beta and AT8 markers to detect dystrophic neurites. Immunohistochemistry and surface quantification indicate that there are less dystrophic neurites around the Aβ plaques in the Lyn deficient 5XFAD mouse brain than the control 5XFAD (Fig. 6A, B). For cognitive assays, Barnes maze latency and Novel object recognition (NOR) tests were performed. We found decreased times to goal box in the Barnes maze and increased time with novel objects in the NOR for 5XFAD X Lyn$^{-/-}$ mice compared to 5XFAD (Fig. 6C, D). Both the 5XFAD X Lyn$^{-/-}$ and 5XFAD mice performed worse in both cognitive tests compared to WT, as would be expected. Additionally, we assessed the neuronal cell count in WT, 5XFAD, and 5XFADXLyn$^{-/-}$ mice using flow cytometry and discovered that the absence of Lyn restores the neuronal cell population compared to 5XFAD (Fig. 6E, F).

Effects of TLIM on TLR4-Lyn interaction to improve microglial phagocytosis and neuronal dystrophy

To determine a potential role for our TLR4-Lyn interacting modulator (TLIM) proteins, we performed a dose response curve that allowed us to determine the TLIM IC_{50}: 17.9 nM, using GraphPad Prism. That is, when 17.9 nM of TLIM is added to a co-immunoprecipitation between GST-TLR4 and native Lyn kinase, only 50% of the native Lyn will associate with GST-TLR4 (Fig. 7A). TLIM treatment resulted in increased phagocytosis of Aβ as compared to GST control. As proof of principle, additional gating on the DAMs that phagocytosed Aβ-pHrodo was performed to determine the effect of TLIMs on the expression of Lyn and TLR4 (Fig. 7B-E). TLIM treatment results in decreased Lyn expression and increased Aβ phagocytosis. The trans-well experiment was performed to ascertain Lyn's role in neuronal damage (Fig. 7F). TLIM treatment in the microglia-neuron trans-well resulted in reduced dystrophic neurites and restored normal neuronal morphology (Fig. 7G, H).

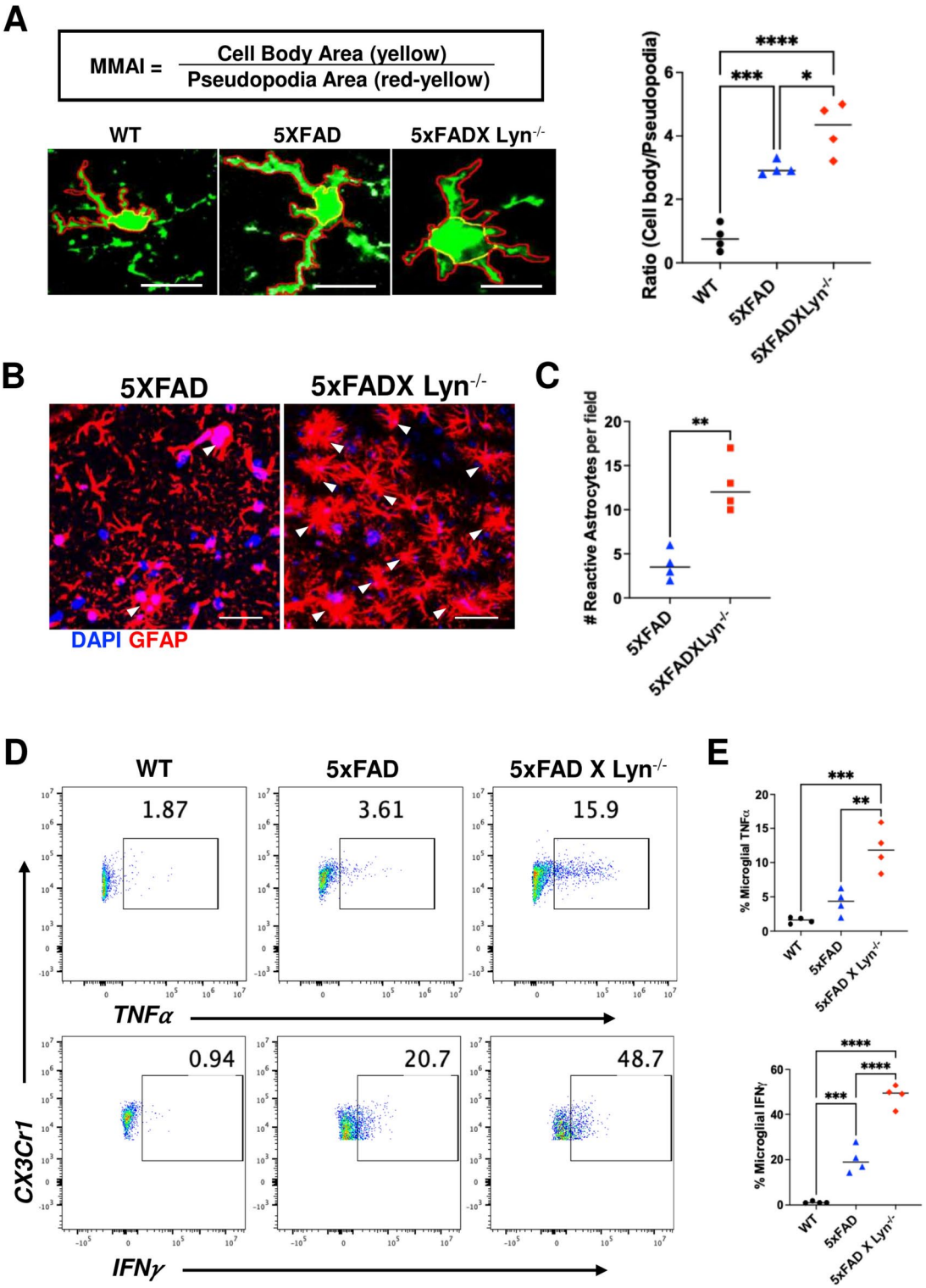

Fig. 3. Microglial morphology analysis and inflammatory cytokine (IFNɣ) production. **a**) The ratio of cell body area to pseudopodia area was calculated and termed microglial morphology analysis index (MMAI), scale bars = 10 µm. Area measurements were done using ImageJ software. n = 4 ; F = 39.82, statistical analysis was done by one-way ANOVA, *P < 0.05, **P < 0.001, ***P < 0.0001 between groups. **b**) IHC imaging of 5xFAD and 5xFAD X Lyn$^{-/-}$mice for GFAP (1:500; red), counterstained with DAPI (blue), scale bars = 50 µm. **c**) Quantification of reactive astrocytes (GFAP^{+}) per field (n = 4; Student's t-test *P < 0.05 between groups). Flow analysis of TNFα and IFNɣ production by microglia, characterized by CD11b^{+}CD45^{med} populations of WT, 5XFAD and 5XFAD X Lyn$^{-/-}$ mouse brains. **e**) Quantification of TNFα (F = 25.48) and IFNɣ (F = 114) production by the MG (n = 4; One-way ANOVA *P < 0.05, **P < 0.001, ***P < 0.0001 between groups).

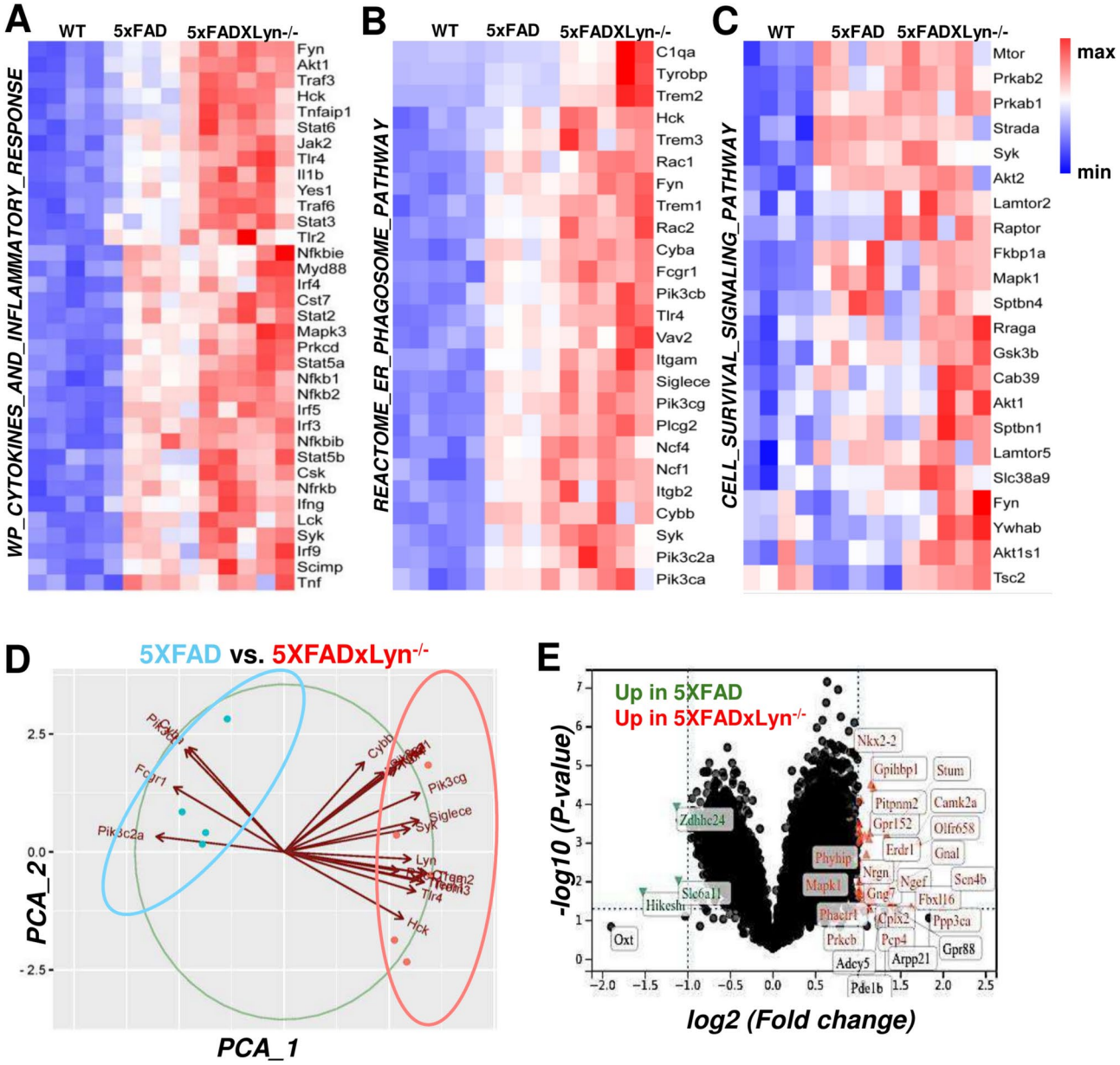

Fig. 4. Spatial transcriptomics analysis of microglia specific genes and functional pathways. Heatmaps generated by gene set enrichment analysis (GSEA) of set of signature genes expression in the microglia of WT, 5XFAD and 5XFAD X Lyn$^{-/-}$ mice involved in **a**) inflammatory cytokine signaling pathway and **b**) microglial phagocytosis pathways **c**) cell signaling pathway **d**) primary component analysis (PCA) plot on the genes involved in phagocytosis in 5XFAD and 5XFAD X Lyn$^{-/-}$**e**) volcano plot compares the microglial gene upregulation in 5XFAD and 5XFAD X Lyn$^{-/-}$ mouse.

Discussion

Our current work demonstrates the importance of microglial TLR4-Lyn signaling in Alzheimer's disease. Although both sexes are utilized for all the experiments, we did not find significant differences between the sexes in the outcomes we measured, thus the samples were pooled. First, TLR4 and Lyn kinase have a direct, protein–protein interaction established by co-immunoprecipitation. Second, this interaction increases in a 5XFAD mouse compared to WT, in support of our previous findings[41]. Interestingly, we also found that the majority of Disease associated microglia (DAMs), as assessed by CD11c^{+}Clec7a^{+}, expressed increased levels of TLR4 and activated Lyn kinase. Together these findings indicate that TLR4 and activated Lyn kinase increasingly associate in response to AD pathology and may represent the more active or "M1-like" component of DAMs (Fig. 1). To further evaluate the role of Lyn kinase in AD, we generated Lyn kinase deficient 5XFAD mice by crossing 5XFAD and global Lyn knockout strains. The increased expression of Syk, phospho-Syk, AkT, phospho-GSK3β, and PI3K kinases in the absence of Lyn suggests that Syk-PI3K mediated protection is negatively regulated by Lyn

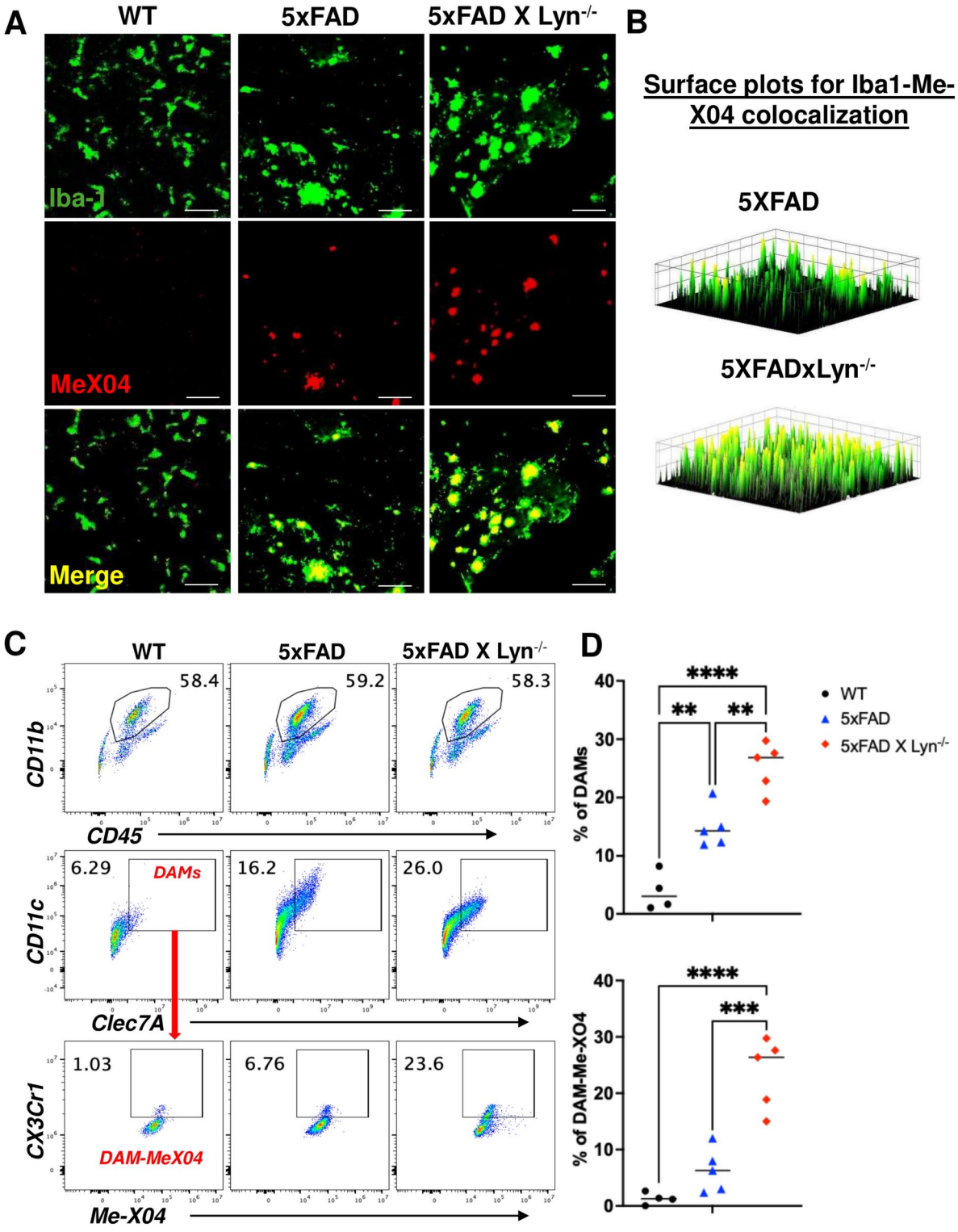

Fig. 5. In vivo phagocytosis of Aβ in WT, 5xFAD and 5xFAD X Lyn$^{-/-}$ mouse brain cells. **a**) Immunostaining of Iba-1 (green), Aβ oligomers were bound to the IP administered methoxy-X04 (Me-X04) (red), all scale bars = 50 μm **b**) Surface plots for Iba1-Me-X04 colocalization. **c**) in vivo Aβ phagocytosis measured by Tmem119^{+}Me-X04^{+} population gated on DAMs (CD11c^{+}Clec7a^{+}), plotted on microglia (CD11b^{+}CD45^{med}). Data analyzed by FlowJo; **d**) Quantification of DAMs (F = 37.70) and DAM Aβ phagocytosis (F = 31.32). (n = 4; One-way ANOVA *P < 0.05, **P < 0.001, ***P < 0.0001 between groups).

kinase in in 5XFAD mice. We confirmed these data using both western blot, immunohistochemistry, and flow cytometry (Fig. 2).

Further supporting the assertion that Lyn kinase inhibits inflammation, analysis of microglial morphology demonstrated that the cell body area to pseudopodia area also increased from WT to 5XFAD to 5XFAD X Lyn$^{-/-}$ (Fig. 3A). More directly, we also measured inflammatory cytokines produced by microglia using flow cytometry and found increased secretion of IFNγ and TNFα from WT to 5XFAD to 5XFAD X Lyn$^{-/-}$ (Fig. 3D, E). We next sought to elucidate the effect of global Lyn kinase deletion on astrocytes due to their essential role in modulating neuronal activity[42,43]. Similar to microglia, astrocytes are now recognized to exist across a spectrum of activation and varying phenotypes. Reactive astrocytes refer to those that undergo changes in their structure, molecular composition, and function in response to CNS injury, disease, or infection[44]. Glial fibrillary acidic protein (GFAP), an important protein found in the intermediate filaments of astrocytes, is the most widely used marker to identify reactive astrocytes. Elevated levels of GFAP in brain tissues, especially in diseased or injured areas, are recognized as a sign of astrocyte activation and proliferation[45,46]. Thus, in our current study, we found that global deletion of Lyn yielded an increased number of reactive astrocytes, compared to 5XFAD control mice (Fig. 3B, C). Current evidence suggests minimal expression of Lyn in astrocytes[47–49]; therefore, the increase in reactive astrocytes could have one of two explanations. Either Lyn deletion in microglia results in more activated microglia communicating with astrocytes to induce a more inflammatory astrocyte phenotype, or Lyn is expressed in astrocytes and the transformation into a more reactive astrocyte phenotype is direct. Further experiments are required to make this determination; however, the overall theme is consistent, Lyn inhibits inflammatory phenotypes.

Our unbiased spatial transcriptomic analysis shows an increased expression of the genes involved in the AD inflammation, Aβ phagocytosis, and cell survival signaling pathways in the 5XFAD X Lyn$^{-/-}$ brains compare to 5XFAD (Fig. 4). Immunohistochemistry and Flow cytometry analysis of in vivo Aβ phagocytosis demonstrates that the absence of Lyn kinase increases the DAM population and enhances DAM-Aβ phagocytosis (Fig. 5). The inverse relationship between Lyn expression and DAM-Aβ phagocytosis, may be mediated by inhibition of microglial Syk based on our data from Fig. 2.

To translate our findings on the effects of Lyn, we demonstrated that 5XFAD X Lyn$^{-/-}$ mice have fewer dystrophic neurites, improved memory on the Barnes maze, and improved recognition on the novel object test. This again suggests that Lyn is inhibiting the protective functions of TLR4-mediated inflammation and the subsequent Syk-mediated cell survival pathways (Figs. 2&6). Finally, our novel TLR4-Lyn interacting modulator (TLIM) proteins that compete for the interaction site between TLR4 and Lyn, demonstrate efficacy in increasing conversion of macrophages to a DAM phenotype and phagocytosis of Aβ, while reducing expression of Lyn and dystrophic neurites (Fig. 7). Thus, TLIMs, in this model seem to inhibit Lyn function, similar to what was seen in 5XFAD X Lyn$^{-/-}$ (Fig. 7C). Taken together, we believe that microglial Lyn is inhibiting the protective functions of microglial Syk in 5XFAD mice, specifically, inflammation, Aβ phagocytosis, and metabolic fitness. Furthermore, our TLIM in vitro shows promise via modulating of the TLR4-Lyn pathway which could be beneficial in Alzheimer's disease.

Methods

ARRIVE guidelines adherence

All experiments conformed to the ARRIVE guidelines for in vivo research[50]. These features ensure that our design is rigorous to deliver robust and unbiased results. Equal numbers of male and female mice were used, and no mice were excluded from analysis.

Animals

6-month-old 5xFAD adult mice (Jax stock # 034,848) and their wild type (WT) age and sex-matched littermates were studied and bred with Lyn$^{-/-}$ for creating the 5XFADxLyn$^{-/-}$ mice. This overall study was conducted with 8 animals in each group (n = 8). The animals were purchased from Jackson laboratory and were housed under a 12-h light/12-h dark cycle-specific pathogen free conditions. All animal experiments detailed herein complied with the regulations formulated by the Institutional Animal Care and Use Committee (IACUC) of the Cooper University Health Care (23–015).

Immunoblotting

Protein determination was performed using 3 mice per group. Mouse brain lysates from all the groups were prepared using RIPA lysis buffer. Total protein concentrations in both in vitro and iv vivo lysates were measured using Bicinchoninic acid assay (BCA) method and were equally loaded into 4–20% pre-cast gradient gels (Bio-Rad, Cat# 4,561,083). Following gel run, proteins were transferred onto PVDF membrane (Millipore, Cat# IPFL00005) using Trans-Blot Turbo™ system (Bio-Rad). Next, the membrane was blocked in blotting grade blocker (Bio-Rad 1,706,404; 5% w/v in 0.1% TBST). To probe for phospho-proteins, blocking step was performed in 3% BSA-TBST. After blocking membrane was incubated with mouse anti-TLR4 (1:1000, Invitrogen, Cat# 14–9041-80), rabbit anti-phospho-Lyn (1:1000 Bioss, Cat# bs-3257R), rabbit anti-Lyn (1:1000, CST, Cat# 2796S), rabbit anti-phospho-Syk (1:1000, CST, Cat# 2710), rabbit anti-Syk (1:1000, CST, Cat# 2712), rabbit anti-pi3k (1:1000, CST, Cat# 4292), rabbit anti-Akt (1:1000, CST, Cat# 4691), rabbit anti-phospho-Akt (1:1000, CST, Cat# 4060), rabbit anti-phosho-GSK3β (1:1000, CST, Cat# 9323), rabbit anti-GSK3β (1:1000, CST, Cat# 12,456) and rabbit anti-GAPDH (1:1000, CST, Cat# 2118S), antibodies. After overnight incubation at 4 °C with primary antibodies, membranes were washed thrice in 0.1%TBST and incubated with goat anti-rabbit IgG (1:20,000, Invitrogen, Cat# 31,460) and goat anti-mouse IgG (1:20,000, Invitrogen, Cat# 31,430) ECL secondary antibodies for 1 h at RT. Phospho antibodies were diluted in 3% BSA-TBST while all other antibodies were diluted in 5%

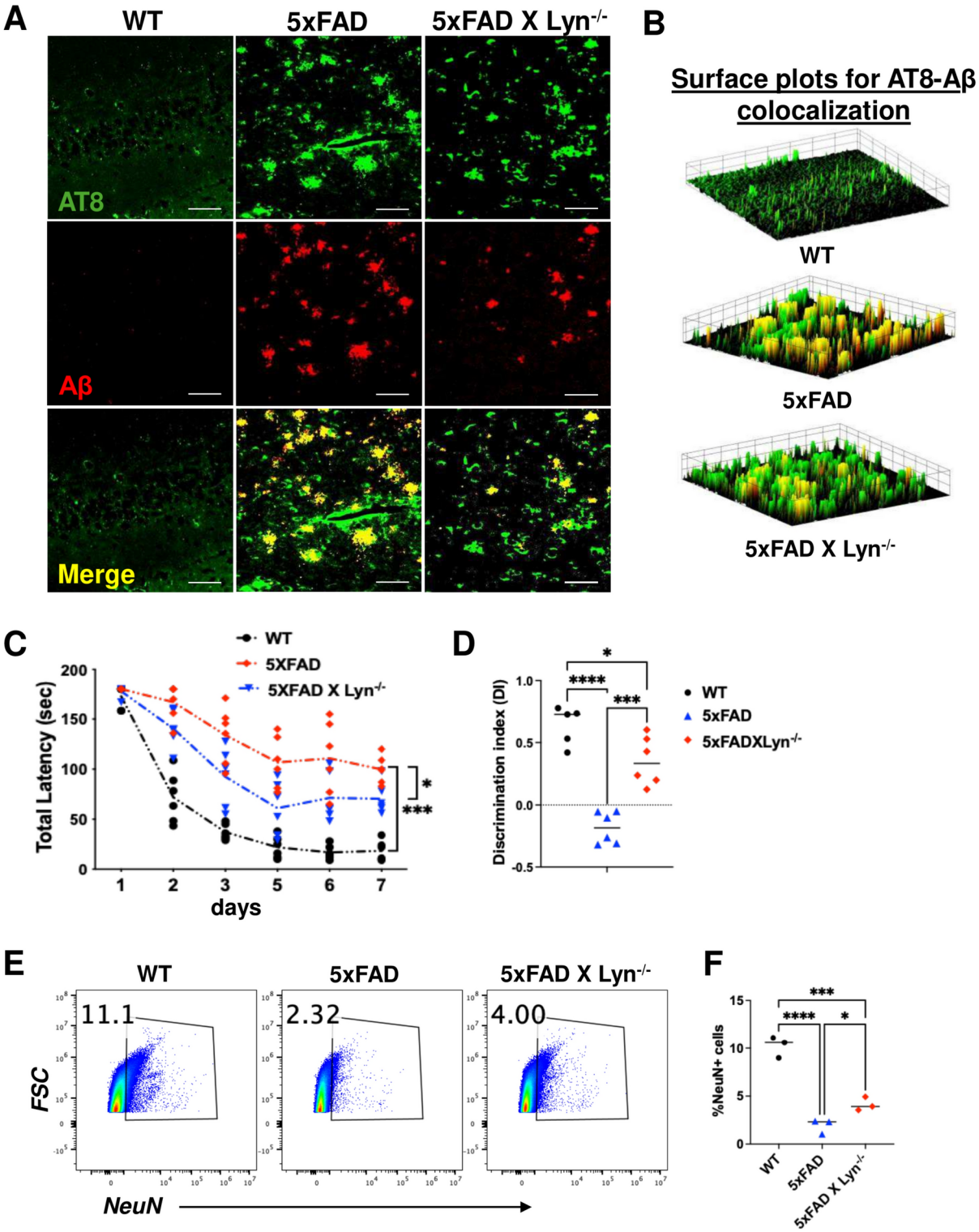

blotting grade blocker. Membranes were visualized by chemiluminescence on Bio-Rad Chemi-doc system. The images were analyzed in image lab software.

IP and co-IP

The mouse brains used for co-immunoprecipitation were homogenized in 1XRIPA buffer with 1XProtease inhibitor cocktail (PIC). The in vitro microglia cultures were trypsinized and cells were pellet, n = 3. Cell lysis was performed in RIPA buffer containing PIC. The whole cell lysate protein concentration was determined via BCA assay. Then following homogenization, the lysate was centrifuged at 2,900 × g for 20 min at 4 °C. The supernatant was then taken and centrifuged for 45 min at 29,000Xg and 4 °C. Lyn and MyD88 were co-immunoprecipitated with TLR4 IP. For this, 20 µl of a 50% protein AG-Sepharose beads (Pierce Invitrogen) slurry was added to control and experimental tubes. The beads were washed in PBS and incubated with 3ug of rabbit anti-TLR4

◀**Fig. 6**. Lyn controls neuronal dystrophy and cognitive dysfunction in AD. **a**) Immunostaining to determine dystrophic neurites around the Aβ plaque. WT, 5xFAD and 5xFAD X $Lyn^{-/-}$ mouse brain cortical sections were stained with AT8 (green) for phosphorylated tau (p-tau) and Aβ (red). All scale bars = 50 µm. **b**) Surface plots for AT8-Aβ colocalization. **c**) Cognitive function test by Barnes maze (F = 54.80, 2-way ANOVA where the 2 variables are time and genotype to assess for differences amongst all groups and Bonferroni post hoc test to assess for differences between pairs of groups). **d**) Discrimination index measured by Novel object recognition test (F = 37.23, One way ANOVA). n = 6; *P < 0.05, **P < 0.001, ***P < 0.0001 were considered statistically significant. **e**) Flow analysis to determine the neuronal population in the brain cells using anti-mouse NeuN, a neuronal marker. **f**) Quantification of neuronal cell percentage in the mouse brain by measuring $Neun^{+}$ cells, n = 3; F = 52.10, One-way ANOVA to assess for differences amongst all groups and Bonferroni post hoc test to assess for differences between pairs of groups. *P < 0.05, **P < 0.001, ***P < 0.0001 was considered statistically significant.

antibodies (CST, Cat# 14,358) or 3ug rabbit pre immune serum for 15 min at room temperature. The mixture was spun down for 5 s, and the supernatant was discarded. 940 µl of PBS was then added to each tube along with 780 µg of mouse brain or microglia lysate prepared as described above and incubated with constant mixing at 4 °C overnight. The tubes were then spun down at 10,000Xg and washed with 500 µl of PBS five times. Immunoprecipitated proteins were then eluted with 50 µl of Laemmli buffer. 20 µl of the eluted samples and 5 µl of lysate were loaded and resolved by SDS-PAGE and subjected to western blot/immunoblot analysis as described above.

Immunohistochemistry

Mouse brains were fixed with 4% PFA by cardiac perfusion, then collected and embedded in OCT, each group consisted of 4 mice. Fresh frozen brains were cryosectioned into 10 µm serial coronal sections with a Leica CM3050 S cryostat. Next, the brain slices were permeabilized with 0.1% Tween-20 in PBS, blocked with 10% normal goat serum for 1 h at RT and stained overnight at 4 °C with primary antibodies. To understand the TLR4-Lyn association we performed double staining with rabbit monoclonal Lyn (1:500, Cell Signaling Tech. Cat# 5568) and mouse monoclonal TLR4 (1:500, Cell Signaling Tech. Cat# 41,134) with DAPI (Vector, Cat# 561,483) counterstaining. Dystrophic neurites and hyperphosphorylated tau were observed by staining with mouse monoclonal AT8 (1:500, Invitrogen, Cat# MN1020) and rabbit monoclonal A-beta (1:500, Cell Signaling Tech. Cat# 8243S). To examine the reactive astrocytes, brains slices were co-stained with GFAP (1:500, Cell Signaling Tech. Cat# 3670S) and DAPI. After overnight incubation with primary antibodies at 4 °C, brains slices were washed with 0.1%TBST and incubated with goat anti-rabbit-488 (1:350, Invitrogen, Cat# A-11008) and goat anti-mouse IgG (1:500, Invitrogen, Cat# A-21422) secondary antibodies for 1 h at RT. All imaging was done with a Nikon A1R HD25 inverted confocal microscope. Co-localization histograms were generated using the coloc-2 feature of ImageJ software. Blue represents the lowest population overlap frequency possible while yellow represents the highest. Lower the slope for each heat map, more the co-localization per staining. Lab personnel interpreting the immunostaining were not aware of the groups from whence they came.

Flow cytometry

Mouse brain cells were isolated using debris removal solution as described previously[51]. Flow cytometry was carried out using 4 mice in each group. For analyzing, freshly prepared mouse CNS cells were washed, resuspended in FACS buffer and were incubated with mouse TruStain FcX Fc-receptor blocker (1:50, BioLegend, Cat# 422,302) to block non-specific sites. Further the cells were stained with APC-CY7-CD11b (1:100, BioLegend, Cat# 101,226), PB-CD45 (1:100, BioLegend, Cat# 103,126), FITC-CX3CR1 (1:100, BioLegend, Cat# 149,020), PE-CY7 Tmem119 (1:100, eBioscience, Cat# 25–6119-82), AF700-CD11c (1:100, BioLegend, Cat# 117,320), PE-CLEC7A (1:100, BioLegend, Cat# 144,304), APC-pLyn (1:100, CST, Cat# 78,740), and PerCP-Cy5.5-TLR4 (1:100, Bioss, Cat# bs-1021R) using fluorophore-conjugated monoclonal antibodies. Microglia and macrophages were identified by gating $CX3Cr1^{hi}Tmem119^{hi}$ and $CX3Cr1^{hi}Tmem119^{lo}$ on the $CD11b^{+}CD45^{med}$population, respectively. Further the DAMs and non-DAMs macrophages were detected by $CD11c^{+}CLEC7a^{+}$ populations gated on the microglia and macrophages. TLR-Lyn expressions then measured by DAMs-$TLR4^{+}Lyn^{+}$ populations. The intracellular cytokine staining was conducted by incubating the freshly prepared brain cell suspension with Invitrogen cell stimulation cocktail for 5 h. Cells were then stained with microglial surface markers (30 min), fixed with 4% PFA (15 min) and stained with PE-dazzle-TNFα (1:100, BioLegend, Cat# 506,346) and PE-CY7-IFNγ (1:100, Tonbo Biosciences, Cat# TB-60–7311-U025). The microglial population was characterized as above. In addition, to look at the neuronal cell population the mouse brain cells were stained with AF-647 conjugated anti-mouse NeuN antibody (1:100, Bio-techne, Cat# NBP1-77,686). The neuronal population were measured by NeuN positive population from all brain cells, here 3 animals were used in each group.

Calculation of microglial morphology

Microglial morphology was quantified using the Microglial morphology Analysis Index (MMAI) as reported previously[39]. MMAI was calculated by dividing the cell body area by the microglial pseudopodia area, in image J (n = 4). To calculate the areas, z-stacks (in vitro 3D cell culture) and 2D images (in vivo mouse brain slices) were split into individual channels. Microglia images color threshold and surface areas were measured after drawing ROIs around the cell body and pseudopodia projections.

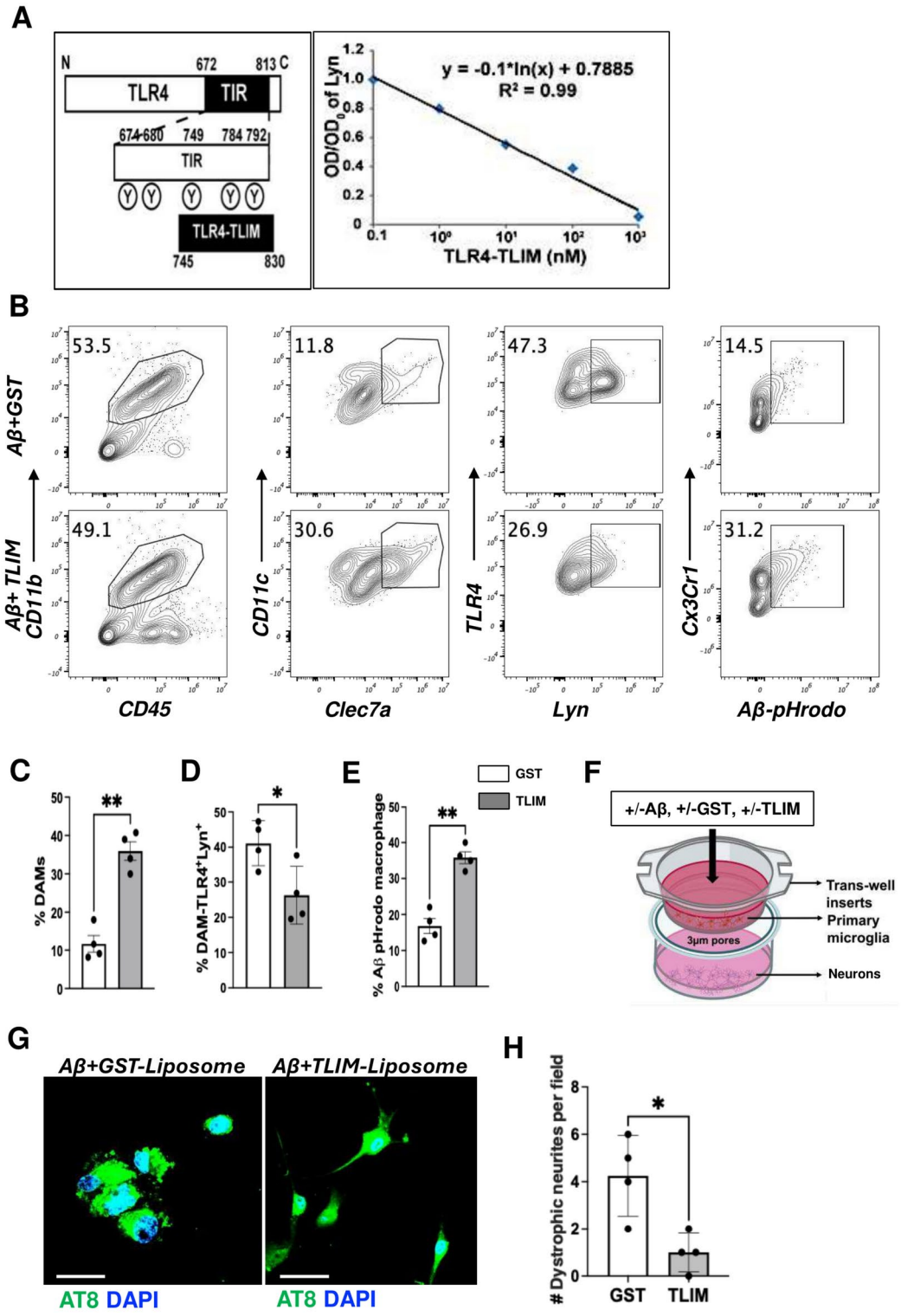

Digital spatial transcriptomics

Frozen brains were fixed with 4% PFA by cardiac perfusion and then were cut in 10-μm serial coronal sections with a Leica CM3050 S cryostat and sent to the University of Minnesota Genomics Center for probe hybridization, IF, region of interest (ROI) selection, sequencing, and data analysis[52,53]. Detailed procedure is explained in supplementary method-S1.

Aβ-phagocytosis assay

In vivo phagocytosis assay was done by intraperitoneal (IP) administration of Methoxy-X04 (Me-X04) (Tocris Bioscience, Cat# 4920) to the mice, as described previously[40]. We used 8 mice in each group for phagocytosis assay, four mice for flow cytometry and four mice for immunohistochemistry. Aβ-phagocytosis was detected by Me-X04 positive DAMs ($CD11c^{+}CLEC7a^{+}$) population. Both flow cytometry and immunohistochemical

◀**Fig. 7**. Effects of TLIM on TLR4-Lyn interaction to improve microglial phagocytosis and neuronal dystrophy. **a**) TLR4 domains, region of interaction (ROI) defining TLR4-TLIM and Dose–response curve for TLR4-TLIM IC50 = 17.9 nM. **b**) Microglial phagocytosis assay; primary microglia were incubated with pHrodo tagged $A\beta_{1\text{-}42}$ oligomers and GST-liposomes or TLIM-liposomes. Data analyzed by FlowJo; n = 4 per group. Quantifications of **c**) DAMs, **d**) $Lyn^{+}TLR4^{+}$ positive DAMs and **e**) DAM-Aβ phagocytosis in GST or TLIM liposome treated AD-microglia cultures (n = 4; Student's t-test *P < 0.05, **P < 0.001 between groups). **f**) Microglia-Neuron Trans-well Assay. Primary microglia (MG) plated on the top chamber and neuronal cell line (hippocampal) plated in the bottom chamber. Cells were incubated with Aβ oligomers for 2 h, followed by 1-h incubation with 20 nM of either GST-liposomes or TLIM-liposomes. **g**) Immunohistochemistry staining of AT8 (green, 1:500) and DAPI (blue) in Aβ treated trans-well cultures. **h**) Quantification of number of dystrophic neurites per filed stained with AT8 (green), scale bars = 25 μm n = 4; Student's t-test *P < 0.05, **P < 0.001 between groups.

analysis were done as described earlier in the method section. For ex-vivo Aβ phagocytosis, primary microglia were incubated with 10 μM synthetic $A\beta_{1\text{-}42}$ oligomers tagged with pHrodo-red (Invitrogen, Cat# P36600). $A\beta_{1\text{-}42}$ oligomers was prepared as reported earlier[54]. Briefly, Aβ (1–42) peptides (Abcam, Cat# 120,959) were resuspended in DMSO, diluted in F12 medium and incubated at 4 °C for 24 h for oligomerization. $A\beta_{1\text{-}42}$ oligomers then spun down at 1600 × g for 2 min and collected pellet was resuspended in PBS. For Aβ-pHrodo labeling, 5ul of pHrodo dye was added to the $A\beta_{1\text{-}42}$ oligomer solution and incubated for 30 min in dark, due to its light-sensitive nature. The pHrodo tagged $A\beta_{1\text{-}42}$ oligomers were washed twice in PBS and the pellet was resuspended in PBS. On the day of experiment, pHrodo tagged Aβ oligomers were added on top of cell culture medium in a final concentration of 500 nm. The primary microglia were allowed 3 days to acclimate, followed by the addition of either TLIM or GST control on day 3 and cells were harvested after 24 h and subjected to flow cytometry. Aβ-pHrodo phagocytosis was detected by pHrodo positive DAMs ($CD11c^{+}CLEC7a^{+}$) population.

Cloning, expression and purification of TLIM

Murine TLR4-Lyn interacting modulator (TLIM) coding region was amplified from mouse cDNA. The amplicons were cloned into pQE-Trisystem vector (Qiagen 32,942). *E. coli* DH5α cells were transformed with TLIM amplicon containing vectors. Plasmids were extracted from transformed cells using PureYield™ Plasmid mini prep system (Promega A1222). Correct clones confirmed by agarose gel electrophoresis and DNA sequencing. Next, BL21DE3 cells were transformed with plasmids checked for presence of TLIM. Primary culture was inoculated with single colony and allowed to grow at 37 °C, 200 rpm for 16 h. Then, secondary culture was initiated by diluting primary culture in 1: 100 ratios in Nutrient broth (Oxoid CM0001). After the culture grew to 0.6 OD_{600}, protein expression was induced by adding 1 mM IPTG to the culture. Culture was continued to grow at 25 °C for 20 h before collecting the bacterial cells by centrifugation. Cells were lysed in B-PER cell lysis buffer (Thermo Fischer, Cat# 78,243) followed by sonication. Cell lysate was separated by centrifugation and filtered through HisPur Ni–NTA columns (Thermo Fischer 88,226) following manufacturer's protocol. Briefly, samples were prepared by mixing in equal volume of equilibration buffer and columns were equilibrated to room temperature (RT). Columns were then washed in equilibration buffer and incubated with sample for 1 h at RT in 4 °C in an end over end tube rotator. Following incubation, columns were washed, and proteins were eluted in elution buffer in 0.5 ml aliquots. OD at 280 nm was measured for all eluted aliquots to check for proteins. Correct protein was confirmed by western blotting with anti-His tag antibodies. Aliquots with TLIM proteins were pooled together and concentrated and buffer exchanged. Purified proteins were stored in 10% glycerol in -80 °C freezer.

Determination of TLIM IC_{50} concentration

To determine the concentration of TLR4-Lyn interacting modulator (TLIM) protein, we performed a dose response curve of TLIM with GST-TLR4 to block interaction with native mouse Lyn. Pull down of Lyn (1:500) by GST-TLR4 (1:1000) was demonstrated using western blotting in the presence of various concentrations of 6xHis-TLR4-TLIM (1:1000). GST-TLR4 was concentrated using Pierce Glutathione Magnetic Beads. TLR4-TLIM with a 6xHis tag was purified from bacterial lysates using a HisPur Ni–NTA Spin Column with 1 mL resin bed, and the following concentrations of purified 6xHis-TLR4-TLIM were added to the GST-TLR4/glutathione magnetic beads: 0.1 nM, 1 nM, 10 nM, 100 nM, 1000 nM. Mouse brain lysate treated with RBCs was then added to each GST-TLR4 on glutathione beads/6xHis-TLR4-TLIM mixture, followed by elution with 50 mM reduced glutathione in PBS (pH = 8.0). The optical density of native Lyn pulled down by GST-TLR4 was graphed against TLR4-TLIM concentration, and a semi-log best fit line is shown, which allowed us to determine the TLIM IC_{50}: 17.9 nM. To test the utility of TLIMs, PMG cultures were incubated with either 20 nM of liposome-encapsulated TLIM OR 20 nM liposome-encapsulated GST (glutathione-S-transferase) protein. GST was chosen as a control to test the utility of TLIMs, we used liposome-encapsulated TLIMs and liposome-encapsulated GST (glutathione-S-transferase) protein both at concentrations of 20 nM, prepared using commercially available liposome kit (Sigma Aldrich, Cat# L4395). To interrogate the TLIM's effect on Aβ phagocytosis in vitro, we used primary microglia from 6-month-old BL/6 mice. We prepared a 10 μM of oligomeric Aβ solution with 5 μM of pHrodo dye for 30 min. pHrodo-red is a pH sensitive dye that increasingly fluoresces as the pH decreases; thus, as Aβ-pHrodo moves from phagosome to lysosome its mean fluorescent intensity increases. Primary microglia were then incubated with Aβ-pHrodo alone for 2 h, followed by incubation with 20 nM of TLIM or GST control for one additional hour.

Trans-well assay

A trans-well assay was performed with the murine primary microglia and mouse neuronal cell lines, where primary microglia were plated in the top chamber, and mouse hippocampal cells were plated in the bottom chamber, n = 3 (Fig. 7F). After 3 days of acclimation, the top and bottom chambers were placed together, and experiments were started. The primary microglial cells were incubated with $A\beta_{1\text{-}42}$ oligomers for 3 h and 20 μM TLIM for 2 h (preparation and concentration explained above). After incubation, immunohistochemistry of neurons in bottom chamber was performed for amyloid and dystrophic neurites.

Statistical analysis

Continuous variables were assessed for normality with skewness and kurtosis. Barnes maze and Three chamber sociability tests were analyzed using two-way ANOVA with Bonferroni's post hoc test. For all other statistical comparisons, multiple experimental groups were compared using one-way ANOVA with Bonferroni's post hoc test, or if two groups were compared a Student's t test was used. Analysis was conducted in GraphPad Prism 10. Differences were considered significant at $P < 0.05$.

No animals were excluded from these results. No significant difference was observed between sexes, so equal numbers of male and female mice were combined to form each group. Confounders were minimized by performing cognitive assessments at the same time of the day to eliminate circadian variation.

DEGs (Differentially Expressed Genes) of GeoMx RNA data between the two groups (5XFAD and 5XFADXLyn$^{-/-}$) were determined by unpaired two-tailed student's t test with fold change > 2 or < 0.5, and $p < 0.05$ was considered statistically significant. The multiple test correction of Benjamini–Hochberg was used to adjust the p-values of individual genes. The volcano plots of DEGs were visualized by Hiplot (https://hiplot.org)[55]. The GOBiological Process enrichment of DEGs were analyzed and visualized using the ClusterProfiler R package in Rstudio[56]. The network of pathways was visualized by ShinyGO[57].

Data availability

The analyzed data of the current study are available from the corresponding author upon reasonable request. The spatial transcriptomic data will be available on public database.

Received: 12 January 2025; Accepted: 28 March 2025
Published online: 03 April 2025

References

1. Al-Ghraiybah, N. F. et al. Glial Cell-Mediated Neuroinflammation in Alzheimer's Disease. *Int. J. Mol. Sci.* https://doi.org/10.3390/ijms231810572 (2022).
2. Kwon, H. S. & Koh, S. H. Neuroinflammation in neurodegenerative disorders: the roles of microglia and astrocytes. *Transl. Neurodegener.* **9**, 42. https://doi.org/10.1186/s40035-020-00221-2 (2020).
3. Li, K., Li, J., Zheng, J. & Qin, S. Reactive Astrocytes in Neurodegenerative Diseases. *Aging Dis.* **10**, 664–675. https://doi.org/10.14336/AD.2018.0720 (2019).
4. Zhang, W., Xiao, D., Mao, Q. & Xia, H. Role of neuroinflammation in neurodegeneration development. *Signal Transduct. Target Ther.* **8**, 267. https://doi.org/10.1038/s41392-023-01486-5 (2023).
5. Katsumoto, A., Takeuchi, H., Takahashi, K. & Tanaka, F. Microglia in Alzheimer's Disease: Risk Factors and Inflammation. *Front. Neurol.* **9**, 978. https://doi.org/10.3389/fneur.2018.00978 (2018).
6. Yang, Y. & Zhang, Z. Microglia and Wnt Pathways: Prospects for Inflammation in Alzheimer's Disease. *Front. Aging Neurosci.* **12**, 110. https://doi.org/10.3389/fnagi.2020.00110 (2020).
7. Islam, R., Choudhary, H., Rajan, R., Vrionis, F. & Hanafy, K. A. An overview on microglial origin, distribution, and phenotype in Alzheimer's disease. *J. Cell Physiol.* **239**, e30829. https://doi.org/10.1002/jcp.30829 (2024).
8. Shippy, D. C., Watters, J. J. & Ulland, T. K. Transcriptional response of murine microglia in Alzheimer's disease and inflammation. *BMC Genomics* **23**, 183. https://doi.org/10.1186/s12864-022-08417-8 (2022).
9. Cameron, B. & Landreth, G. E. Inflammation, microglia, and Alzheimer's disease. *Neurobiol. Dis.* **37**, 503–509. https://doi.org/10.1016/j.nbd.2009.10.006 (2010).
10. Combs, C. K. Inflammation and microglia actions in Alzheimer's disease. *J. Neuroimmune Pharmacol.* **4**, 380–388. https://doi.org/10.1007/s11481-009-9165-3 (2009).
11. Chetelat, G. et al. Amyloid imaging in cognitively normal individuals, at-risk populations and preclinical Alzheimer's disease. *Neuroimage. Clin.* **2**, 356–365. https://doi.org/10.1016/j.nicl.2013.02.006 (2013).
12. Sturchio, A. et al. High cerebrospinal amyloid-beta 42 is associated with normal cognition in individuals with brain amyloidosis. *EClinicalMedicine* **38**, 100988. https://doi.org/10.1016/j.eclinm.2021.100988 (2021).
13. Deczkowska, A. et al. Disease-Associated Microglia: A Universal Immune Sensor of Neurodegeneration. *Cell* **173**, 1073–1081. https://doi.org/10.1016/j.cell.2018.05.003 (2018).
14. Dhib-Jalbut, S. et al. Neurodegeneration and neuroprotection in multiple sclerosis and other neurodegenerative diseases. *J. Neuroimmunol.* **176**, 198–215. https://doi.org/10.1016/j.jneuroim.2006.03.027 (2006).
15. Ferreira, S. A. & Romero-Ramos, M. Microglia Response During Parkinson's Disease: Alpha-Synuclein Intervention. *Front. Cell Neurosci.* **12**, 247. https://doi.org/10.3389/fncel.2018.00247 (2018).
16. Keren-Shaul, H. et al. A Unique Microglia Type Associated with Restricting Development of Alzheimer's Disease. *Cell* **169**, 1276–1290. https://doi.org/10.1016/j.cell.2017.05.018 (2017).
17. Hu, Y. et al. Replicative senescence dictates the emergence of disease-associated microglia and contributes to Abeta pathology. *Cell Rep.* **35**, 109228. https://doi.org/10.1016/j.celrep.2021.109228 (2021).
18. Fang, F. et al. RAGE-dependent signaling in microglia contributes to neuroinflammation, Abeta accumulation, and impaired learning/memory in a mouse model of Alzheimer's disease. *FASEB J.* **24**, 1043–1055. https://doi.org/10.1096/fj.09-139634 (2010).
19. Hickman, S., Izzy, S., Sen, P., Morsett, L. & El Khoury, J. Microglia in neurodegeneration. *Nat. Neurosci.* **21**, 1359–1369. https://doi.org/10.1038/s41593-018-0242-x (2018).
20. Walker, D. G. & Lue, L. F. Immune phenotypes of microglia in human neurodegenerative disease: Challenges to detecting microglial polarization in human brains. *Alzheimers Res. Ther.* **7**, 56. https://doi.org/10.1186/s13195-015-0139-9 (2015).
21. Paudel, Y. N. et al. Impact of HMGB1, RAGE, and TLR4 in Alzheimer's Disease (AD): From Risk Factors to Therapeutic Targeting. *Cells* https://doi.org/10.3390/cells9020383 (2020).

22. Yu, J. T. et al. Common variants in toll-like receptor 4 confer susceptibility to Alzheimer's disease in a Han Chinese population. *Curr. Alzheimer Res.* **9**, 458–466. https://doi.org/10.2174/156720512800492495 (2012).
23. Azam, S. et al. Regulation of Toll-Like Receptor (TLR) Signaling Pathway by Polyphenols in the Treatment of Age-Linked Neurodegenerative Diseases: Focus on TLR4 Signaling. *Front. Immunol.* **10**, 1000. https://doi.org/10.3389/fimmu.2019.01000 (2019).
24. Boutajangout, A. & Wisniewski, T. The innate immune system in Alzheimer's disease. *Int. J. Cell Biol.* **2013**, 576383. https://doi.org/10.1155/2013/576383 (2013).
25. Opal, S. M. et al. Effect of eritoran, an antagonist of MD2-TLR4, on mortality in patients with severe sepsis: the ACCESS randomized trial. *JAMA* **309**, 1154–1162. https://doi.org/10.1001/jama.2013.2194 (2013).
26. Lowell, C. A. Src-family and Syk kinases in activating and inhibitory pathways in innate immune cells: Signaling cross talk. *Cold Spring Harb. Perspect. Biol.* https://doi.org/10.1101/cshperspect.a002352 (2011).
27. Parsons, S. J. & Parsons, J. T. Src family kinases, key regulators of signal transduction. *Oncogene* **23**, 7906–7909. https://doi.org/10.1038/sj.onc.1208160 (2004).
28. Nygaard, H. B., van Dyck, C. H. & Strittmatter, S. M. Fyn kinase inhibition as a novel therapy for Alzheimer's disease. *Alzheimers Res. Ther.* **6**, 8. https://doi.org/10.1186/alzrt238 (2014).
29. Nygaard, H. B. et al. A phase Ib multiple ascending dose study of the safety, tolerability, and central nervous system availability of AZD0530 (saracatinib) in Alzheimer's disease. *Alzheimers Res. Ther.* **7**, 35. https://doi.org/10.1186/s13195-015-0119-0 (2015).
30. Colonna, M. & Wang, Y. TREM2 variants: New keys to decipher Alzheimer disease pathogenesis. *Nat. Rev. Neurosci.* **17**, 201–207. https://doi.org/10.1038/nrn.2016.7 (2016).
31. Konishi, H. & Kiyama, H. Microglial TREM2/DAP12 Signaling: A Double-Edged Sword in Neural Diseases. *Front. Cell Neurosci.* **12**, 206. https://doi.org/10.3389/fncel.2018.00206 (2018).
32. Wang, S. et al. TREM2 drives microglia response to amyloid-beta via SYK-dependent and -independent pathways. *Cell* **185**, 4153–4169. https://doi.org/10.1016/j.cell.2022.09.033 (2022).
33. Ennerfelt, H. et al. SYK coordinates neuroprotective microglial responses in neurodegenerative disease. *Cell* **185**, 4135–4152. https://doi.org/10.1016/j.cell.2022.09.030 (2022).
34. Scapini, P., Pereira, S., Zhang, H. & Lowell, C. A. Multiple roles of Lyn kinase in myeloid cell signaling and function. *Immunol. Rev.* **228**, 23–40. https://doi.org/10.1111/j.1600-065X.2008.00758.x (2009).
35. Lamagna, C., Scapini, P., van Ziffle, J. A., DeFranco, A. L. & Lowell, C. A. Hyperactivated MyD88 signaling in dendritic cells, through specific deletion of Lyn kinase, causes severe autoimmunity and inflammation. *Proc. Natl. Acad. Sci. U S A* **110**, E3311-3320. https://doi.org/10.1073/pnas.1300617110 (2013).
36. Ban, T. et al. Lyn Kinase Suppresses the Transcriptional Activity of IRF5 in the TLR-MyD88 Pathway to Restrain the Development of Autoimmunity. *Immunity* **45**, 319–332. https://doi.org/10.1016/j.immuni.2016.07.015 (2016).
37. Nunes de Miranda, S. M., Wilhelm, T., Huber, M. & Zorn, C. N. Differential Lyn-dependence of the SHIP1-deficient mast cell phenotype. *Cell Commun. Signal* **14**, 12. https://doi.org/10.1186/s12964-016-0135-0 (2016).
38. Xiao, W. et al. Positive and negative regulation of mast cell activation by Lyn via the FcepsilonRI. *J. Immunol.* **175**, 6885–6892. https://doi.org/10.4049/jimmunol.175.10.6885 (2005).
39. Islam, R. et al. Development of a 3D Brain Model to Study Sex-Specific Neuroinflammation After Hemorrhagic Stroke. *Transl. Stroke Res.* https://doi.org/10.1007/s12975-024-01243-y (2024).
40. Lau, S. F., Wu, W., Seo, H., Fu, A. K. Y. & Ip, N. Y. Quantitative in vivo assessment of amyloid-beta phagocytic capacity in an Alzheimer's disease mouse model. *STAR Protoc.* **2**, 100265. https://doi.org/10.1016/j.xpro.2020.100265 (2021).
41. Islam, R., Rajan, R., Choudhary, H., Vrionis, F. & Hanafy, K. A. Gender differences in Alzheimer's may be associated with TLR4-LYN expression in damage associated microglia and neuronal phagocytosis. *J. Cell Physiol.* **239**, e30916. https://doi.org/10.1002/jcp.30916 (2024).
42. Liu, Z. et al. Beneficial effects of gfap/vimentin reactive astrocytes for axonal remodeling and motor behavioral recovery in mice after stroke. *Glia* **62**, 2022–2033. https://doi.org/10.1002/glia.22723 (2014).
43. Lawrence, J. M., Schardien, K., Wigdahl, B. & Nonnemacher, M. R. Roles of neuropathology-associated reactive astrocytes: a systematic review. *Acta Neuropathol. Commun.* **11**, 42. https://doi.org/10.1186/s40478-023-01526-9 (2023).
44. Escartin, C. et al. Reactive astrocyte nomenclature, definitions, and future directions. *Nat. Neurosci.* **24**, 312–325. https://doi.org/10.1038/s41593-020-00783-4 (2021).
45. Brahmachari, S., Fung, Y. K. & Pahan, K. Induction of glial fibrillary acidic protein expression in astrocytes by nitric oxide. *J. Neurosci.* **26**, 4930–4939. https://doi.org/10.1523/JNEUROSCI.5480-05.2006 (2006).
46. Eng, L. F., Vanderhaeghen, J. J., Bignami, A. & Gerstl, B. An acidic protein isolated from fibrous astrocytes. *Brain Res.* **28**, 351–354. https://doi.org/10.1016/0006-8993(71)90668-8 (1971).
47. Chu, E. et al. Regulation of Microglial Signaling by Lyn and SHIP-1 in the Steady-State Adult Mouse Brain. *Cells* https://doi.org/10.3390/cells12192378 (2023).
48. Ingley, E. Functions of the Lyn tyrosine kinase in health and disease. *Cell Commun. Signal* **10**, 21. https://doi.org/10.1186/1478-811X-10-21 (2012).
49. Stettner, M. R. et al. Lyn kinase activity is the predominant cellular SRC kinase activity in glioblastoma tumor cells. *Cancer Res.* **65**, 5535–5543. https://doi.org/10.1158/0008-5472.CAN-04-3688 (2005).
50. Percie du Sert, N. et al. Reporting animal research: Explanation and elaboration for the ARRIVE guidelines 2.0. *PLoS Biol* **18**, e3000411. https://doi.org/10.1371/journal.pbio.3000411 (2020).
51. Bordt, E. A. et al. Isolation of Microglia from Mouse or Human Tissue. *STAR Protoc.* https://doi.org/10.1016/j.xpro.2020.100035 (2020).
52. Mendiola, A. S. et al. Defining blood-induced microglia functions in neurodegeneration through multiomic profiling. *Nat. Immunol.* **24**, 1173–1187. https://doi.org/10.1038/s41590-023-01522-0 (2023).
53. Wang, Y. et al. Targeting Src SH3 domain-mediated glycolysis of HSC suppresses transcriptome, myofibroblastic activation, and colorectal liver metastasis. *Hepatology* https://doi.org/10.1097/HEP.0000000000000763 (2024).
54. Stine, W. B., Jungbauer, L., Yu, C. & LaDu, M. J. Preparing synthetic Abeta in different aggregation states. *Methods Mol. Biol.* **670**, 13–32. https://doi.org/10.1007/978-1-60761-744-0_2 (2011).
55. Li, J. et al. Hiplot: A comprehensive and easy-to-use web service for boosting publication-ready biomedical data visualization. *Brief Bioinform.* https://doi.org/10.1093/bib/bbac261 (2022).
56. Yu, G., Wang, L. G., Han, Y. & He, Q. Y. clusterProfiler: An R package for comparing biological themes among gene clusters. *OMICS* **16**, 284–287. https://doi.org/10.1089/omi.2011.0118 (2012).
57. Ge, S. X., Jung, D. & Yao, R. ShinyGO: A graphical gene-set enrichment tool for animals and plants. *Bioinformatics* **36**, 2628–2629. https://doi.org/10.1093/bioinformatics/btz931 (2020).

Acknowledgements

We would like to the University of Minnesota Genomics Centers (UMGC) for spatial transcriptomic services.

Author contributions

R. Islam and H. Choudhary performed the experiments and generated data. All other authors contributed to the development and design of the concepts in the article, attended the biweekly meetings, drafted, or critically revised the article for important intellectual content. K. Hanafy provided overall direction and management. R. Islam and K. Hanafy together wrote the manuscript.

Funding

The study was supported by the National Institutes of Health (NIH) Grant R01NS109174-01, Cooper University Health, and Cooper Medical School at Rowan University given to Khalid A. Hanafy, MD, PhD.

Declarations

Competing interests

The authors declare no competing interests.

Additional information

Supplementary Information The online version contains supplementary material available at https://doi.org/10.1038/s41598-025-96456-y.

Correspondence and requests for materials should be addressed to K.H.

Reprints and permissions information is available at www.nature.com/reprints.

Publisher's note Springer Nature remains neutral with regard to jurisdictional claims in published maps and institutional affiliations.